



Anisotropic hemp-stem-derived biochar supported phase change materials with efficient solar-thermal energy conversion and storage

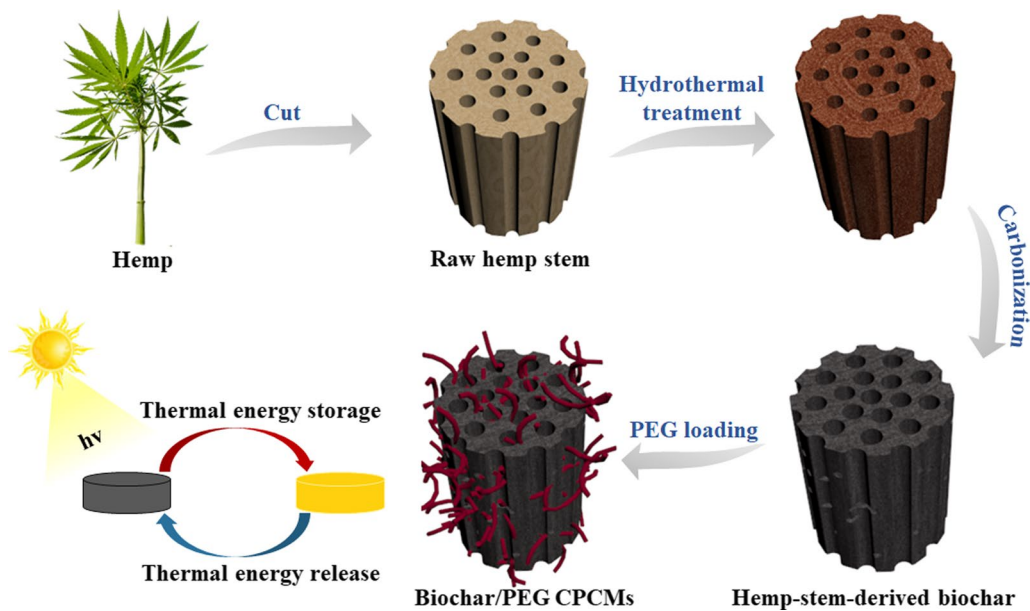
Ruiying Yang¹ · Xiran Guo¹ · Haotian Wu¹ · Weizhi Kang¹ · Kun Song¹ · Yaqiong Li¹ · Xiubing Huang¹ · Ge Wang¹

Received: 21 March 2022 / Accepted: 6 June 2022
© The Author(s) 2022

Abstract

As cheap and renewable sources, the exploitation of biomass resources was of great value in phase change energy storage. In this study, hemp stems were converted into biochars with three-dimensional multi-level anisotropic pores through a temperature-controlled charring process, which were used as supports for polyethylene glycol (PEG6000) to form shape-stable composite phase change materials (ss-CPCMs). It is shown that the ss-CPCMs using anisotropic hemp-stem-derived biochar obtained at a carbonization temperature of 900 °C as a support has high PEG6000 loading rate (88.62wt%), large latent heat (170.44 J/g) and favorable thermal stability owing to its high surface area and hierarchical pores. The biochar-based ss-CPCM also has good light absorption ability with a maximum solar-thermal conversion efficiency of 97.70%. In addition, the different thermal conductivities in the transverse and longitudinal directions of ss-CPCMs reflect the unique anisotropic structure. This work can not only improve the high-value utilization of biochars, but also provide the ss-CPCMs with excellent performance for solar-thermal conversion and storage systems.

Graphical Abstract



Highlights

1. Anisotropic hemp-stem-derived biochar is used as supports of ss-CPCMs.
2. Biochar-supported CPCMs show high PEG loading, latent heat and solar-thermal conversion efficiency.
3. Biochar-supported CPCMs exhibit enhanced anisotropic thermal conductivity and durability.

Keywords Biochar · Phase change materials · Anisotropic structure · Solar-thermal conversion

1 Introduction

In recent years, with the worldwide economic development and the environmental pollution and energy depletion caused by population expansion, improving energy efficiency has attracted extensive attention. In order to alleviate the energy crisis, converting renewable solar energy into thermal energy and storing it for reuse has attracted extensive studies (Alva et al. 2017; Tang et al. 2021). Latent heat thermal energy storage (LHTES) realizes thermal energy storage or release by phase change materials (PCMs) with the characteristics of basically constant temperature and high energy storage density (Aftab et al. 2021), which have been widely used in building (Rathore and Shukla 2021), greenhouse (Chen et al. 2018), solar energy storage (Shi et al. 2021), electronic devices (Tomizawa et al. 2016) and other fields. In this regard, organic solid–liquid PCMs are considered as one of the most promising PCMs because of their controllable phase change temperature, no obvious undercooling and phase separation, no corrosivity and low price (Umair et al. 2019). Nevertheless, despite their promising applications, organic solid–liquid PCMs have some obvious shortcomings, including low thermal conductivity and easy leakage during the melting process, which dramatically restrict their practical applications.

To overcome these challenges, porous materials with large specific surface area, high porosity and good adsorption properties can be used as carriers for the preparation of shape-stable composite phase change materials (ss-CPCMs) (Huang et al. 2019a, b; Yang et al. 2019). The surface tension, capillary forces and hydrogen bonding forces of the porous carriers can effectively restrain the PCMs in the pores (Li et al. 2021a, b). Up to now, various kinds of porous materials such as metallic foams (Zhang et al. 2021a, b), graphene aerogel (Li et al. 2020a, b, c), mesoporous silicas (Li et al. 2022a), metal–organic frameworks (Wang et al. 2018) and expanded graphite (Yuan et al. 2021) have been reported as supports of ss-CPCMs. Especially, porous carbon materials have been widely used to construct multifunctional ss-CPCMs because of their high PCM loading, high thermal conductivity and

extraordinary solar absorption ability (Chen et al. 2021). However, traditional porous carbon materials such as carbon nanotube, graphene oxide and graphene aerogel have problems including high price, complicated preparation process and environmental pollution (Tong et al. 2019; Yang et al. 2018). In the last few years, biomass-based or derived porous carbon materials have gained much attention in terms of their rich porous structures, wide source of raw materials and simple preparation processes (Gabhi et al. 2020; Huang et al. 2019b, a; Qiu et al. 2019).

In terms of solar-thermal energy conversion and storage, the carbonization of biomass to biochar not only has a rich porous structure, but also has increased graphitization and good light absorption capacity, leading to improved thermal conductivity as well as solar-thermal conversion efficiency of ss-CPCMs (Li et al. 2022b; Pan et al. 2021; Sari et al. 2020; Umair et al. 2020). Zhao et al. prepared honeycomb porous biochar from potatoes and radishes and the CPCMs using these as scaffolds were able to load 85.36% of polyethylene glycol (PEG) (Zhao et al. 2018). Li et al. prepared ss-CPCMs with the melting enthalpy of 149 J/g based on three-dimensional spongy eggplant-derived porous carbon and PEG (Li et al. 2020a, b, c). To enhance the thermal conductivity, Zhang et al. instead coated the surface of eggplant-based porous carbon with nano-Ag, which increased the thermal conductivity by 40.9% compared to the CPCM without the nano-Ag particles (Zhang et al. 2021a, b). Atinafu et al. pyrolyzed wheat straw at 550 °C and subsequently loaded *n*-eicosane (ES) separately. However, only a 37.1% loading content of ES with a melting enthalpy (75.0 J/g) was obtained (Atinafu et al. 2021). Therefore, compared with the reported vegetable-derived and other biomass-derived biochars with high price or low PCM load, the porous biochars prepared from biomass resources with rich source, low price and high PCM load are more in line with the needs of sustainable development. Taking good advantages of biowaste to transform it into high value-added products can not only alleviate the energy crisis and environmental pollution, but also increase the comprehensive benefits (Kung et al. 2015, 2014a, 2014b; Li et al. 2020a, b, c).

Hence, in this study, anisotropic hemp-stem-derived porous biochars were fabricated by hydrothermal carbonization, freeze-drying, and high-temperature carbonization. New biochar-based ss-CPCMs were prepared through vacuum impregnation method with carbonized hemp stems (CH) and PEG6000 as raw materials. With optimal carbonization temperature at 900 °C, the prepared ss-CPCM simultaneously integrates good thermal reliability, high thermal energy storage density (170.44 J/g), excellent solar-thermal conversion efficiency (97.70%), and improved thermal conductivity. Meanwhile, the radial and longitudinal heat transfer capabilities of ss-CPCMs demonstrate the anisotropic thermal conductivity path. This research takes full advantages of the porous structure of hemp stems as well as their renewable nature to develop a green path for solar-thermal energy conversion and storage. This also provides new approaches to broaden the high-value utilization of biomass-derived biochars in thermal energy storage.

2 Materials and methods

2.1 Materials

The raw hemp stem was purchased from Taobao E-Shop. PEG with an average molecular weight of 6000 was provided by Shanghai Yuanye Biotechnology Co. Ltd. (Shanghai, China). All other chemical reagents used were of analytical grade and were not further purified.

2.2 Preparation of carbonized hemp stems

The hemp-stem-derived biochars with hollow porous scaffold were synthesized by simple carbonization process, as shown in Fig. 1. Specifically, the hemp stem was divided into about 3 cm sections and moved to a Teflon-lined autoclave, which was left in a 180 °C oven setting for 10 h. After hydrothermal carbonization samples were washed several times to remove surface impurities, then frozen in liquid nitrogen and dried in a freeze dryer for 72 h. Afterwards, the dewatered hemp stem segments were carbonized in a tube furnace at different temperatures (600, 700, 800, 900, 1000 °C) for 1 h under a flowing nitrogen atmosphere at a heating rate of 2 °C/min. The samples were naturally cooled to room temperature to obtain carbonized hemp stems (CH), which were marked as CH-600, CH-700, CH-800, CH-900 and CH-1000, respectively.

2.3 Preparation of CH/PEG ss-CPCMs

As shown in Fig. 1, the ss-CPCMs were prepared by vacuum impregnation method using CH and PEG6000 as raw materials. At first, CH scaffolds with different carbonation temperatures were placed into a centrifuge tube separately with an excess of PEG6000 solid, where PEG6000 was located on top of CH. Thereafter, the centrifuge tubes were placed in a vacuum drying oven at 80 °C and held for 4 h to allow the molten PEG to penetrate into the pores of CH. After vacuum impregnation, the samples were first transferred to filter paper and then transferred into a blast drying oven at 80 °C to get rid of the surplus PEG from the surface of CH. The filter paper was repeatedly changed until no molten PEG leaked. The obtained CH/PEG ss-CPCMs using CH obtained at different carbonization temperatures were named as CPCM-600, CPCM-700, CPCM-800, CPCM-900 and CPCM-1000, respectively. As a control, the uncarbonized hemp stem loaded with PEG was labeled as CPCM-0.

2.4 Characterizations

The structural morphology of the products was characterized by scanning electron microscopy (SEM, SU8000, Japan Hitachi) and TEM (JEM-2100F). Raman spectroscopy (Finder Vista) was applied to analyze the degree of graphitization of CH. The pore size distribution and pore structure parameters of the CH were measured using an automatic mercury injection apparatus (USA Mack corporation Auto Pore IV 9510). The specific surface area of biochars was obtained on a TriStar II 3020 (Micromeritics Instrument Corporation, USA) at 77 K. X-ray photoelectron spectroscopy (XPS) (ESCALAB 250Xi instrument) was applied to study the composition and binding energy of the CH. X-ray diffractometry (XRD, M21X, Cu K α radiation, $\lambda = 1.541 \text{ \AA}$) was employed for the analysis of the phase structure and chemical compatibility of samples. Fourier transform infrared spectroscopy (FTIR, Nicolet 6700 by the KBr pellet technique) was performed in the wave number range 500–4000 cm^{-1} to evaluate the chemical compatibility of the samples. Thermogravimetric analysis (TGA) was obtained on a thermogravimetric analyser (Netzsch STA449F, Germany), heated at a rate of 10 °C/min from 40 to 800 °C under N $_2$ atmosphere. The thermal properties of PEG6000 and ss-CPCMs were studied by differential scanning calorimetry (DSC, Q2000). The thermal conductivity of the composite phase change material was measured using a laser thermal conductivity meter (NETZSCH LFA 467). The thermal management capability of CPCMs was visualized using a thermal imaging camera FLIR ONE Pro.

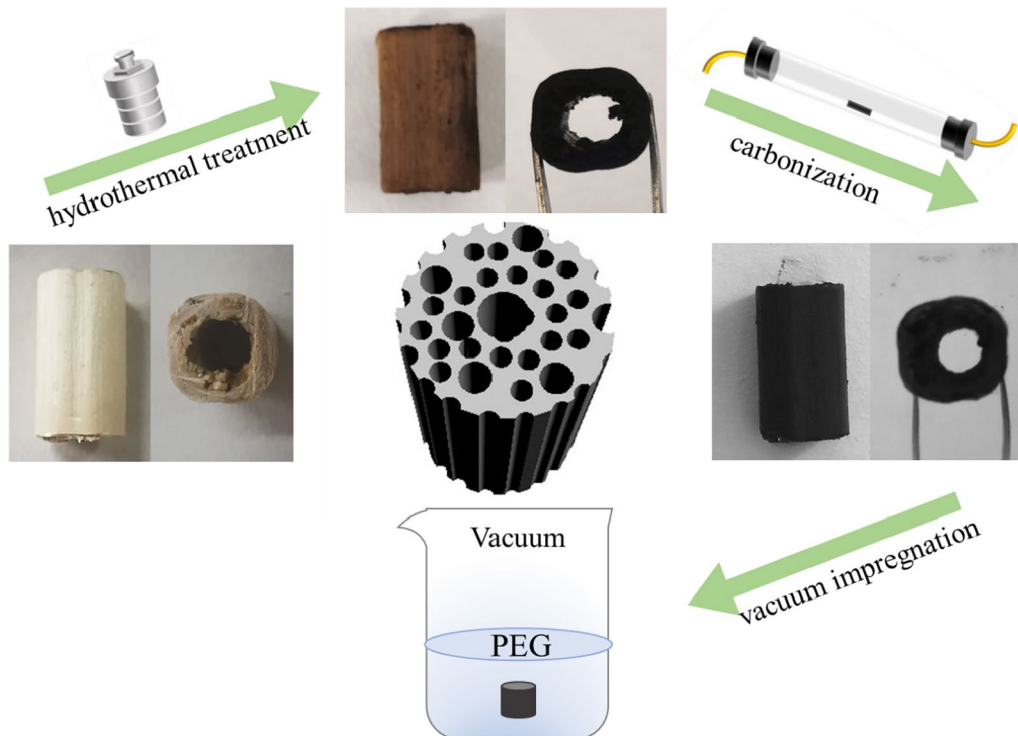


Fig. 1 The schematic diagram for preparation of CH/PEG ss-CPCMs

3 Results and discussion

3.1 Production and characterization of porous carbon scaffolds

The morphological structure of the hemp-stem-derived biochar was recorded by SEM and TEM. From the cross-section of CH (Fig. 2a–e), CH exhibited a porous skeleton structure with distributed pores of different sizes inside, preserving the original porous structure of hemp rods. The porous structure was formed by 5–20 μm small pores around 30–50 μm large circular pores like a honeycomb. With the increasing carbonization temperature, the pore size decreased and the pore distribution became more uniform. CH-900 showed the smallest pore size, more regular pore distribution and thinner pore walls. This was owing to the fact that high temperatures favor the decomposition of cellulose, hemicellulose and other invaginations, resulting in a more developed porous architecture (Song et al. 2020). However, as the carbonization temperature increased to 1000 $^{\circ}\text{C}$, part of the porous structure was destroyed, indicating that the pyrolysis temperature has an important effect on regulating the morphology and porous structure of biochar (Atinafu et al. 2021; Song et al. 2020; Tan et al. 2016). From the longitudinal section of CH (Fig. 2g), it can be observed that the pore channel was nearly through along the growth direction of the hemp rods. Meanwhile, the walls were distributed with circular holes

of 1–2 μm diameter (Fig. 2f, h). Figure 2i shows that some nanopores are also present on the inner and outer surfaces of CH-900. The pores in the wall increased the interconnectivity of the pore channels, which would be favorable to enhance the specific surface area and porosity of CH (Pan et al. 2021; Zhou et al. 2021). All the above results indicate that a multi-level porous structure exists in the resulting biochars, which is beneficial to encapsulate PCM.

Figure 3 presents the pore size distribution curves of hemp stem-derived porous biochars carbonized at different temperatures measured by MIP. Table 1 summarizes the porous structure parameters of carbonized hemp stems at different temperatures. CH was mainly composed of two sizes of large pores with pore sizes ranging from 100 nm to 10 μm and from 15 to 50 μm , respectively. When the charring temperature of CH was increased from 600 to 900 $^{\circ}\text{C}$, the specific surface area increased from 443.58 to 542.25 m^2/g . The average pore size of CH decreased slightly with the increase of carbonization temperature because of the decomposition of some of its components (such as the lignin, cellulose and hemicellulose) at high carbonization temperatures. The higher the carbonization temperature is, the more the porous structure shrinks, and the pore size also decreases (Oginni and Singh 2020). The average porosities of CH-600 to CH-900 were 88.33%, 88.09%, 87.55%, and 87.51%, which revealed that the hemp stem-based biochar contained a rich porous structure. In contrast, further

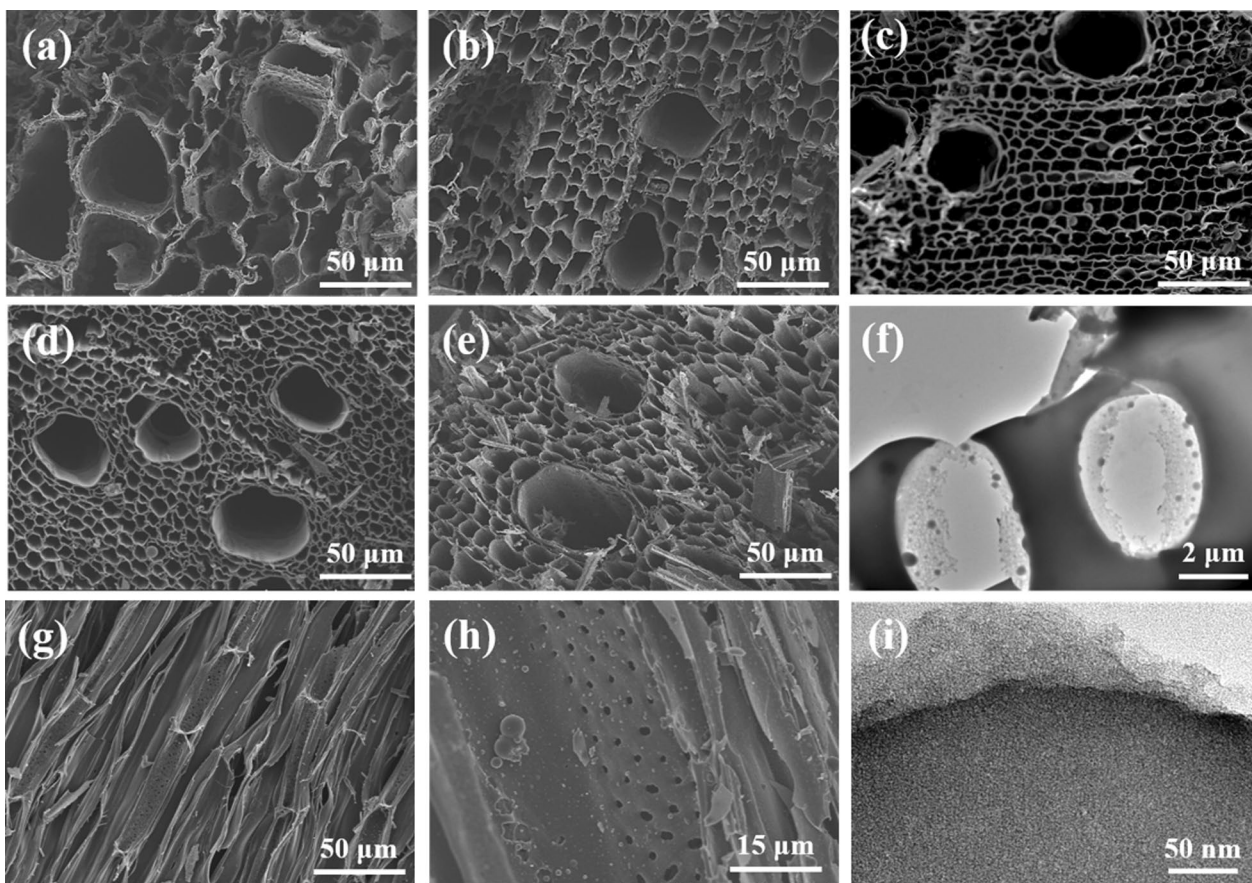


Fig. 2 SEM images of cross sections of **a** CH-600, **b** CH-700, **c** CH-800, **d** CH-900, **e** CH-1000 and **g**, **h** vertical sections of CH-900; TEM images of **f**, **i** CH-900

increasing the carbonization temperature to 1000 °C led to the obviously decreased specific surface area (144.17 m²/g) and slightly reduced porosity (83.43%) of CH-1000, corresponding to the disrupted structure of CH-1000 in the SEM image. In general, CH has wide pore size range and high porosity, which is beneficial to enhance the loading rate of PCM and prevent its leakage.

The surface chemical composition of CH-900 was analyzed by XPS, as shown in Fig. 4a-b. The XPS spectrum of CH-900 (Fig. 4a) shows two peaks at 283.8 and 534.6 eV, corresponding to C 1 s and O 1 s, respectively, where the content of C element is much higher than that of O element (Kim et al. 2022). In the deconvoluted C 1 s XPS spectra of CH-900 (Fig. 4b), the main peak located at a binding energy of 284.8 eV corresponds to the sp² C=C/C-C bond while these peaks with binding energies of 285.7 and 289.1 eV can be assigned to the C-O and O-C=O bands, respectively (Peng et al. 2017).

FT-IR spectroscopy was used to characterize the surface functional groups in these carriers. Absorption peaks were observed at 1094, 1419, 1620, 2920 and 3420 cm⁻¹ for biochars (Fig. 4c). The absorption peak near 1094 cm⁻¹

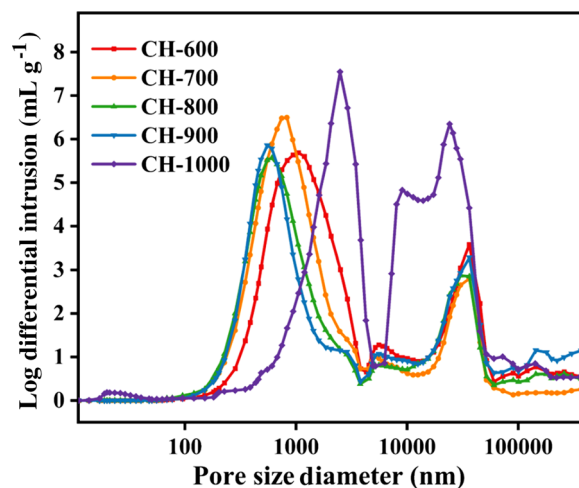


Fig. 3 Aperture distribution curves of CH-600, CH-700, CH-800, CH-900 and CH-1000

was caused by the stretching vibration of C-O, C-C or the bending vibration of C-OH. The absorption peaks around 1419 and 1620 cm⁻¹ correspond to the C=O stretching

Table 1 Microstructural parameters of the hemp-stem-derived porous biochars

Sample	Specific surface area (m ² g ⁻¹)	Average pore diameter (μm)	Porosity (%)
CH-600	443.58	1.25	88.33
CH-700	519.43	0.85	88.09
CH-800	523.82	0.82	87.55
CH-900	542.25	0.92	87.51
CH-1000	144.17	1.19	83.43

vibration, which indicate the presence of a great deal of oxygen-containing functional groups on the carbon material. The strong absorption peak at 3420 cm⁻¹ is the characteristic peak corresponding to hydroxyl O–H. It means that the porous biochar is rich in –OH, which is mainly derived from the hydroxyl groups of carboxylic acids and phenols. In summary, these results show that the hemp stem-derived biochars are an abundant source of oxygen-containing acidic functional groups. XRD was applied to analyze the crystallization properties of hemp stem-derived biochars. As shown in Fig. 4d, all these biochars present two characteristic peaks at 22° and 43°, which correspond to the (002) and (101) crystal planes of graphite crystals, respectively. These two broad diffraction peaks indicate that the main component of the hemp stem-derived biochars is amorphous carbon after high temperature pyrolysis.

To further investigate the degree of graphitization of CH, the prepared biochars were analyzed by Raman spectroscopy. In Fig. 5a, there are two distinct peaks near 1350 cm⁻¹ (D band) and 1580 cm⁻¹ (G band). The D-band was caused by the disorder of the defective graphite structure of the biochar. The G-band, in turn, represented the degree of graphitization of biochar, arising from the sp² hybridization of carbon atoms in the graphite lamellar structure. The intensity ratio (I_D/I_G) between the D-band and G-band indicates the defect density and the degree of graphitization of carbon materials. A smaller ratio indicated a lower degree of defect and disorder and a higher degree of graphitization in the carbon materials (Zhang et al. 2017, 2019). By analyzing the Raman spectra of CH pyrolyzed at different temperatures (Fig. 5b–f), it was found that the I_D/I_G values of biochars were all close to 1.15, showing the presence of graphitic carbon and disordered carbon. Theoretically, the extent of graphitization of carbon materials was positively correlated with the heat treatment temperature. However, raising the carbonization temperature would also introduce more porous structures in CH and increase the number of defects, thus increasing the disorder of the carbon fraction. Thus, the I_D/I_G values of CH were obtained by two mechanisms that check and balance each other (Guo et al. 2016). As a result, the

prepared biochars were amorphous structural carbon with a certain degree of graphitization.

3.2 Morphology and structure of CH/PEG CPCMs

The CPCM-600, CPCM-700, CPCM-800, CPCM-900 and CPCM-1000 were morphologically characterized with SEM. The cross and longitudinal sections of the CPCMs revealed that the multistage porous structure of CH was almost filled with PEG6000 (Fig. 6). Waxy PEG6000 was attached to both the duct and striatal surfaces of CH, and no obvious interface between PEG6000 and CH was noticed. Due to the capillary force and interfacial tension, CH can firmly adsorb and confine PEG6000 in its hierarchical pore channels. The presence of strong hydrogen bonds between biochar and PEG6000 further enhances the stability of PEG6000. The tight integration of PEG6000 and biochar could successfully prevent the leakage of PEG6000 under molten state.

To illustrate the physical and chemical interactions of CH and PEG6000 in the composites, pure PEG6000 and CPCMs were characterized through XRD and FT-IR. As shown in Fig. 7a, pure PEG6000 showed well-defined peaks at 19.0° and 23.0°. The characteristic peaks of CPCMs were basically the same as those of pure PEG6000, and no new peaks appeared, indicating that the crystal structure of PEG6000 did not change before and after impregnation and there was only physical adsorption between PEG6000 and CH. Figure 7b shows the FT-IR spectrum of PEG6000 and CPCMs. The peaks at 3445 and 1112 cm⁻¹ correspond to the characteristic peaks of the stretching vibrations of –OH and C–O of PEG6000, respectively. The absorption peaks at 2887, 1468, 1342, 963, and 832 cm⁻¹ were accounted for C–H stretching and bending oscillations. No new absorption peaks were found in CPCMs, demonstrating that there was only physical interaction between CH and PEG6000 by surface tension, capillary interaction and possible hydrogen bonding. In addition, the XRD patterns and FT-IR spectrum of the biochar-based CPCMs were not significantly varied except for a slight variation in the intensity.

3.3 Thermal performance of CH/PEG CPCMs

In order to analyze the thermal stability and pyrolysis behavior of CPCMs, thermogravimetric analysis was performed. Figure 8 shows the TGA curves of PEG6000 and CPCMs under flowing N₂. There is a one-step thermal degradation in the TGA curve of pure PEG6000, which can be attributed to the breakage of the PEG molecular chain. The decomposition of PEG6000 starts at 350 °C, and the maximum rate of weight loss is at 390 °C. When the temperature reaches 420 °C, PEG6000 decomposes almost completely. The absence of significant weight loss in CPCMs under 350 °C

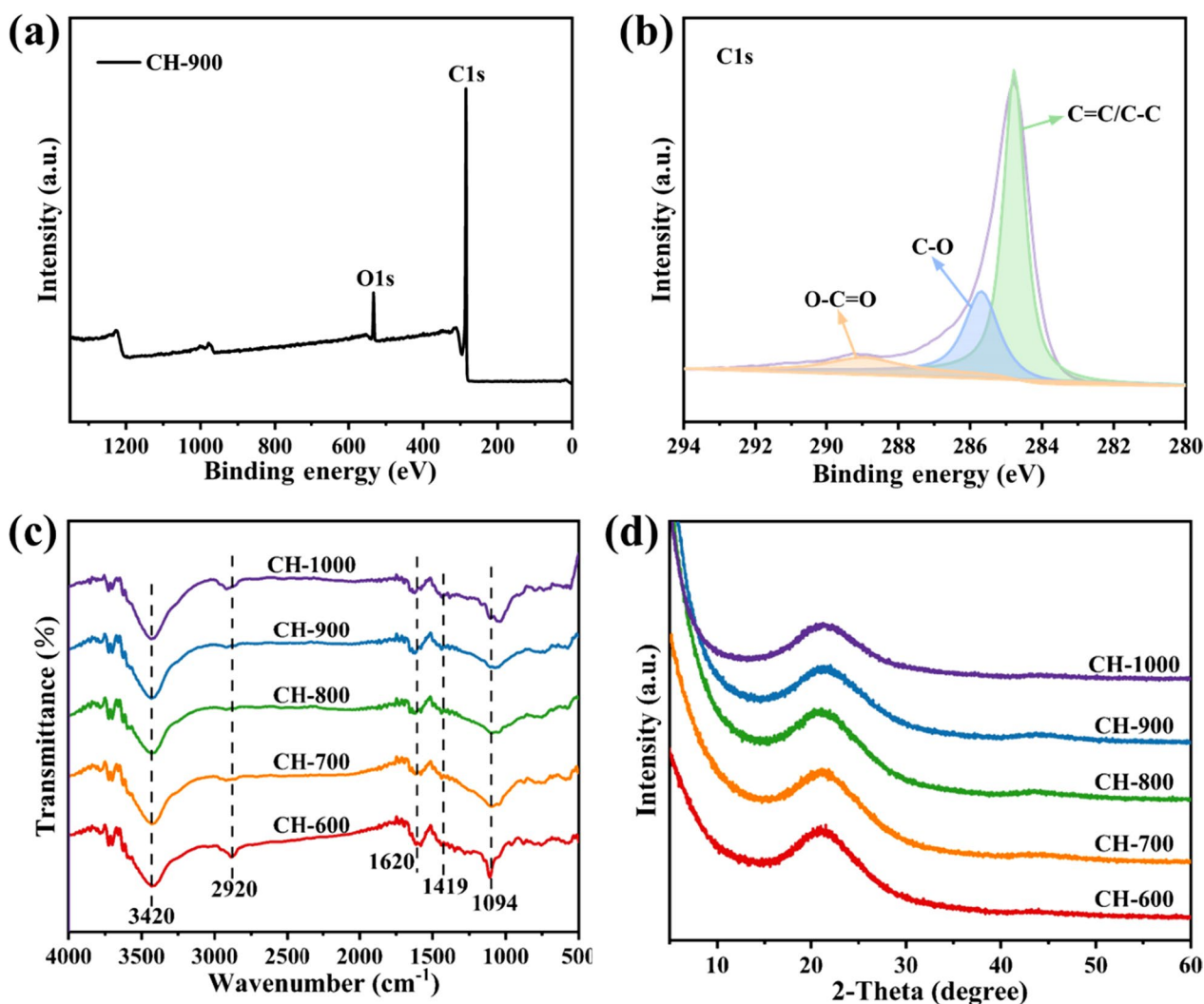


Fig. 4 a XPS survey and b high-resolution C 1 s spectrum of CH-900, c FT-IR spectra and d XRD patterns of CH-600, CH-700, CH-800, CH-900 and CH-1000

indicates that CPCMs have good thermal stability below 350 °C. It can be observed that CPCMs exhibited similar thermal stability to that of PEG6000. Though the mass loss of the CPCMs was mainly from the thermal decomposition of PEG6000, the onset of decomposition temperature was slightly higher than that of PEG6000, which is probably owing to the limited movement of PEG6000 within the biochars. As a whole, CPCMs have good thermal stability up to 350 °C, which is far beyond the working temperature of ss-CPCMs and is beneficial to their practical applications.

The DSC curves of PEG6000, CPCM-600, CPCM-700, CPCM-800, CPCM-900 and CPCM-1000 during melting and cooling are shown in Fig. 9a-b. The corresponding phase change parameters of PEG6000 and CPCMs are listed in Table 2. These CPCMs and pure PEG6000 have similar DSC curves. Nevertheless, the melting temperatures (T_M) of CPCMs are slightly higher than that of pure PEG6000,

which may be attributed to the strong physical adsorption of PEG6000 within biochars through capillary interaction and interfacial tension. The confining effect of the porous structure of CH on PEG6000, and the hydrogen bonding interactions between the biochars and PEG6000 also hindered the thermal diffusion movement of PEG molecular chain segments. These factors together slowed down the phase transition process of confined PEG6000 from the crystalline to the amorphous state in CPCMs (Cao et al. 2022). The slightly lower solidification temperatures (T_S) of CPCMs compared to pure PEG6000 can be due to the restriction of PEG molecular chain movement by the porous carbon network, which in turn limits the crystallization process and leads to a reduction of crystallization segments (Wang et al. 2019). It could be seen from Table 2 that the melting enthalpies (H_M) and solidifying enthalpies (H_S) of CPCMs are both reduced compared to that of pure PEG6000. The melting

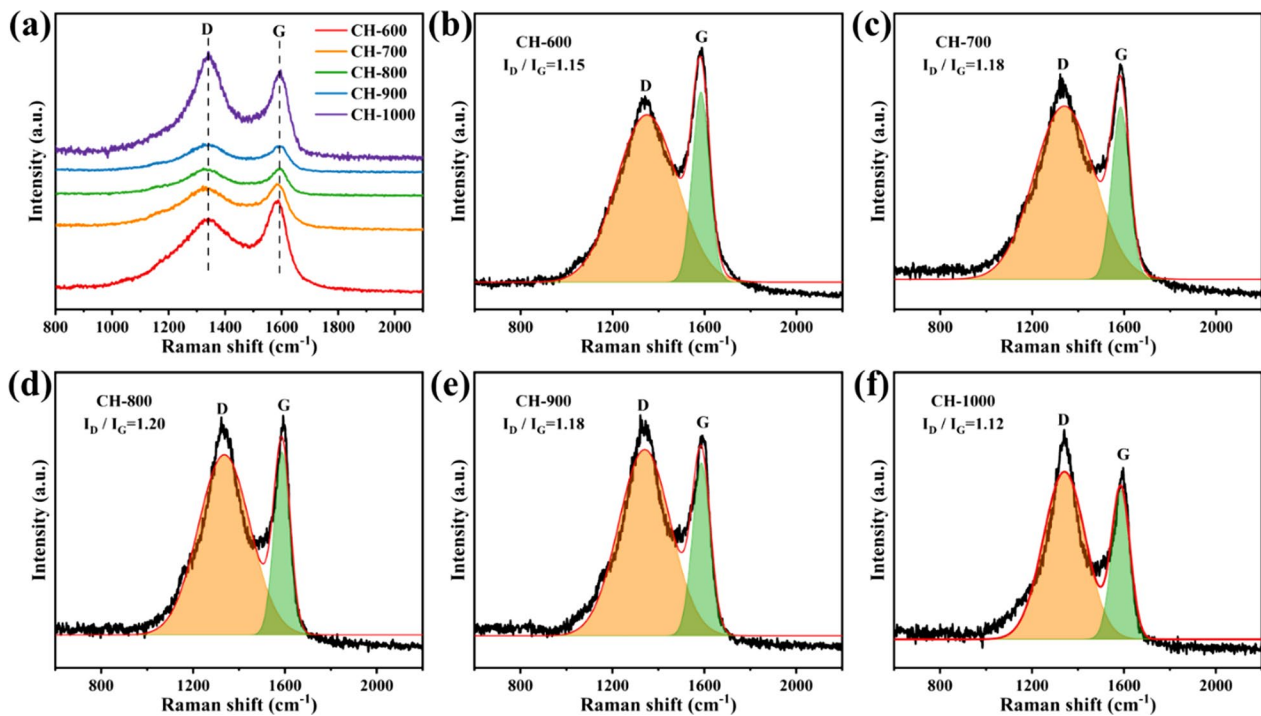


Fig. 5 Raman spectra of CH: **a** general figure, **b** CH-600, **c** CH-700, **d** CH-800, **e** CH-900, and **f** CH-1000

enthalpies of CPCMs first increased from 166.80 J/g of CPCM-600 to 170.44 J/g of CPCM-900 and then decreased to 164.97 J/g of CMCM-1000 with the increase of carbonization temperature, which were consistent with the trend of their porous structures. Moreover, the melting enthalpies of CPCMs were generally higher than their corresponding solidifying enthalpies, which could account for the limited pre-crystallization of some PEG molecular chains adhering to the surfaces of the carrier in the solidifying process (Atinafu et al., 2021). The loading rate φ of CPCMs can be calculated according to Eq. (1):

$$\varphi = \frac{m - m_0}{m} \quad (1)$$

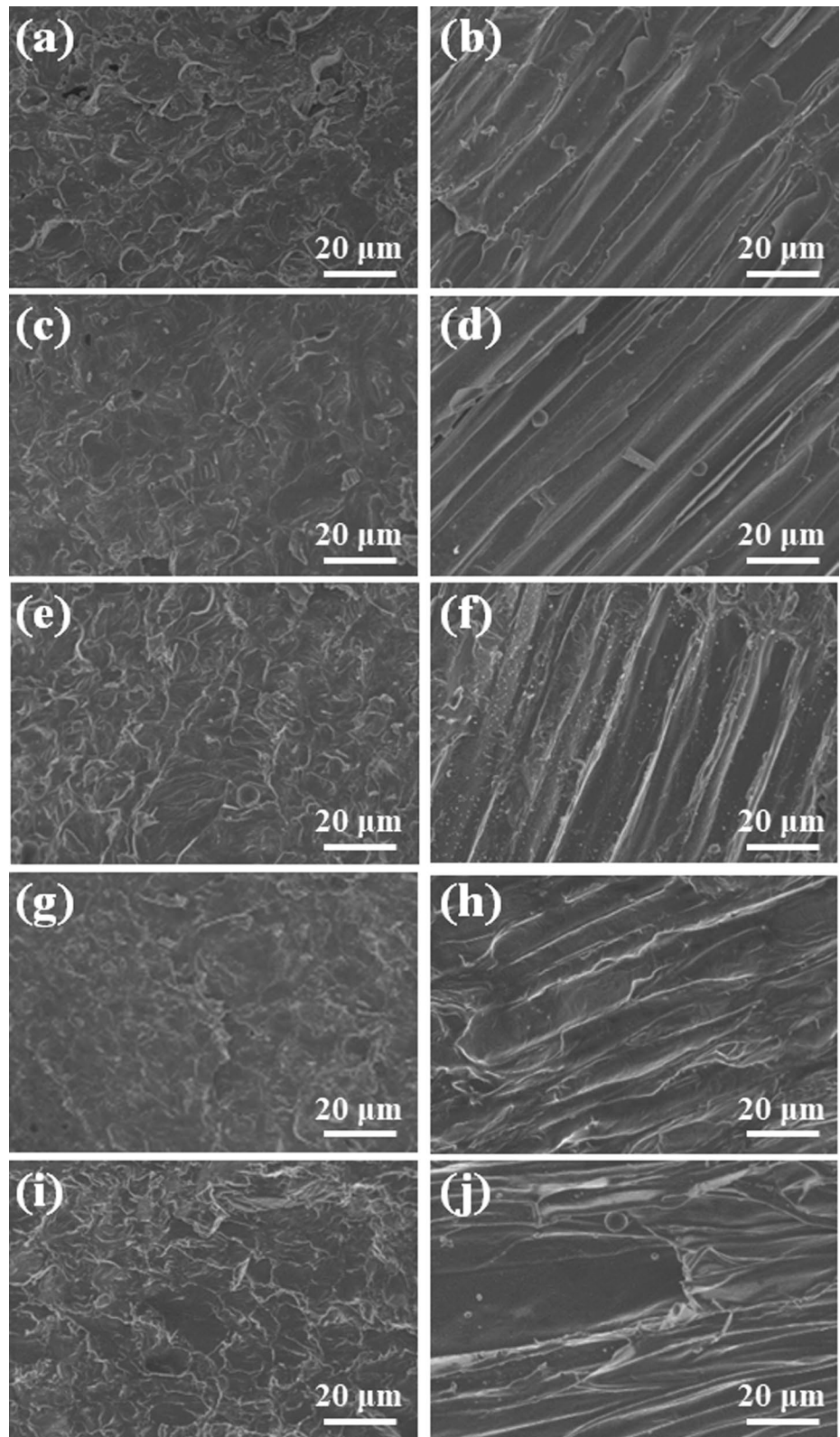
where m is the mass of CPCMs and m_0 is the mass of CH. The loading rates of PEG6000 in CPCM-600, CPCM-700, CPCM-800, CPCM-900 and CPCM-1000 were calculated to be 87.75wt%, 87.51wt%, 87.88wt%, 88.62wt% and 87.79wt%, respectively. The percent impregnation mass of PEG6000 varies due to the structure of the charred hemp stems themselves. In the present work, the melting enthalpy of CPCM-900 was as high as 170.44 J/g and the loading of PEG6000 was 88.62wt%. Compared with the previously reported biomass-based CPCMs (Table 3), the specific surface area of CH-900, the melting enthalpy and loading ratio of PEG in CPCM-900 in this work are relatively higher. Based on the above analysis, it could be concluded that

the CPCM with CH as the support has good heat storage capacity.

The thermal conductivities of pure PEG6000, lateral CPCM-900 and radial CPCM-900 were measured because the pores of CH-900 were grown in a directional manner (Fig. 9c). Compared with the thermal conductivity (0.26 W/mK) of pure PEG6000, the thermal conductivities of CPCM-900 were improved to 0.29 W/mK in the lateral direction and 0.32 W/mK in the radial direction, which can be attributed to the accelerated heat transfer in the composites by the interconnected carbon skeleton and pore channels of CH. However, the enhancement of the thermal conductivity of the CPCM-900 was slight, which was mainly caused by the high loading of PEG6000. Interestingly, the thermal conductivity of CPCM-900 in the radial direction was higher than that in the lateral direction, which is consistent with the porous structure of the CH directional growth. As a result, CH with interconnected hierarchical porous structures could not only act as a support material for encapsulating PCM, but also provide efficient heat transfer channels.

Thermal cycling stability is another essential feature of ss-CPCMs for practical applications. The thermal reliability of CPCM was investigated by conducting 50 melting-solidifying cycle tests on CPCM-900. As can be seen from the DSC curves before and after cycling (Fig. 9d), the DSC curves of CPCM-900 before and after the 50 cycles almost overlap. Despite a slight decrease in the enthalpy of phase change after 50 cycles, the slight change could be negligible

Fig. 6 SEM images of cross sections of **a** CPCM-600, **c** CPCM-700, **e** CPCM-800, **g** CPCM-900 and **i** CPCM-1000; and vertical sections of **b** CPCM-600, **d** CPCM-700, **f** CPCM-800, **h** CPCM-900 and **j** CPCM-1000



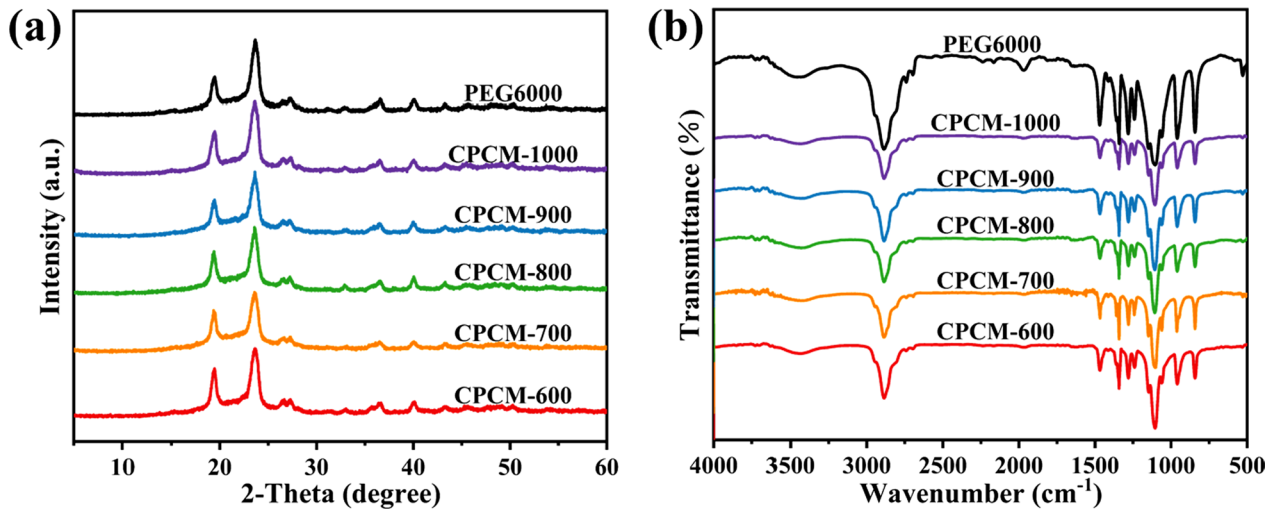


Fig. 7 **a** XRD patterns and **b** FT-IR spectra of PEG6000, CPCM-600, CPCM-700, CPCM-800, CPCM-900 and CPCM-1000

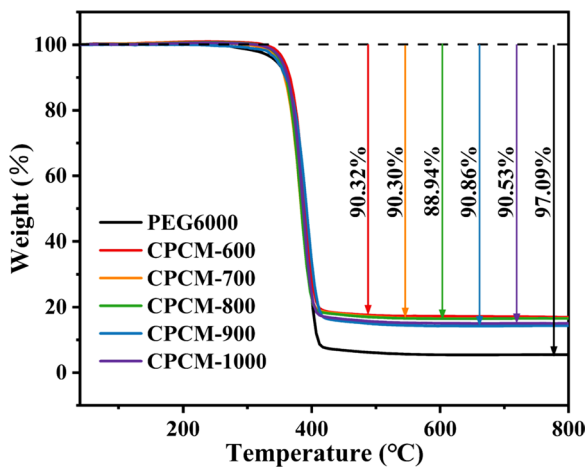


Fig. 8 TGA curves of PEG6000 and CPCMs

compared to the high latent heat of CPCM-900. All the above analysis revealed that the prepared ss-CPCMs could well keep their phase change characteristics and excellent thermal reliability, which could meet the requirements of long-term cycling stability in practical applications.

The solar-thermal conversion performance of these CPCMs was measured using a system consisting of a Xenon lamp light source simulating sunlight, an infrared thermometer, a temperature logger, and a computer (Fig. 10a). Firstly, the sample was placed under Xenon lamp irradiation and the temperature change on its surface was measured in real time by an infrared temperature probe to obtain the time–temperature curve (Fig. 10b). During the first 120 s, the temperature of CPCMs increased rapidly to 55 °C. A temperature plateau appeared in the range of 55–65 °C and

Table 2 Phase change parameters of pure PEG6000 and CPCMs

Sample	PEG content (%)	Melting process		Solidifying process	
		T_M (°C)	H_M (J g ⁻¹)	T_S (°C)	H_S (J g ⁻¹)
PEG6000	100.00	66.34	184.83	39.81	183.47
CPCM-600	87.75	73.95	166.80	37.42	166.92
CPCM-700	87.51	73.76	167.54	36.87	164.41
CPCM-800	87.88	72.36	168.62	39.28	163.60
CPCM-900	88.62	70.52	170.44	39.63	163.86
CPCM-1000	87.79	68.67	164.97	38.63	161.81

lasted for about 200 s, indicating that the heat absorbed by CPCM caused the phase change of PEG6000 at this time. The CPCMs could also store more solar energy, which enabled the CPCMs to reach a maximum temperature of 94 °C. When the light source was turned off, the temperature began to drop rapidly. Once it dropped to about 48 °C, a cooling plateau appeared, demonstrating that the PEG6000 in these CPCMs was continuously releasing heat to prevent its temperature from decreasing, which can be used to regulate the surrounding ambient temperature and thus reduce energy consumption. Based on the physical data of CPCMs and the time–temperature curve, the solar-thermal energy conversion efficiency η can be calculated according to Eq. (2):

$$\eta = \frac{m\Delta H_m}{rs(T_t - T_f)} \quad (2)$$

where m is the mass of the sample, ΔH_m is the melting enthalpy of CPCM, r is the light intensity of simulated sunlight, s is the area of the sample exposed to light, T_t and

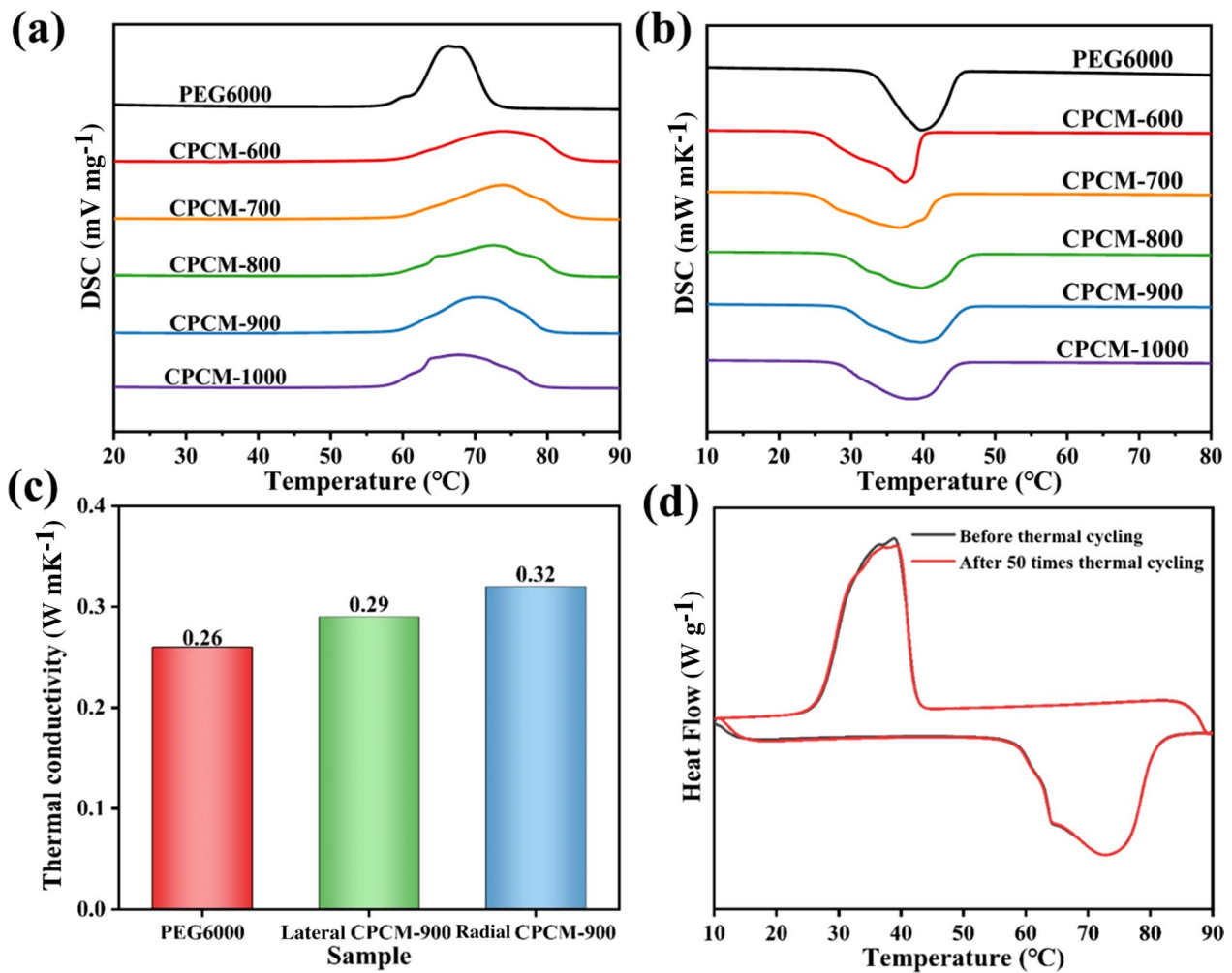


Fig. 9 DSC curves of PEG6000, CPCM-600, CPCM-700, CPCM-800, CPCM-900, CPCM-1000 during heating (a) and cooling (b); (c) Thermal conductivity of the samples; (d) DSC curves before and after 50 cycles of CPCM-900

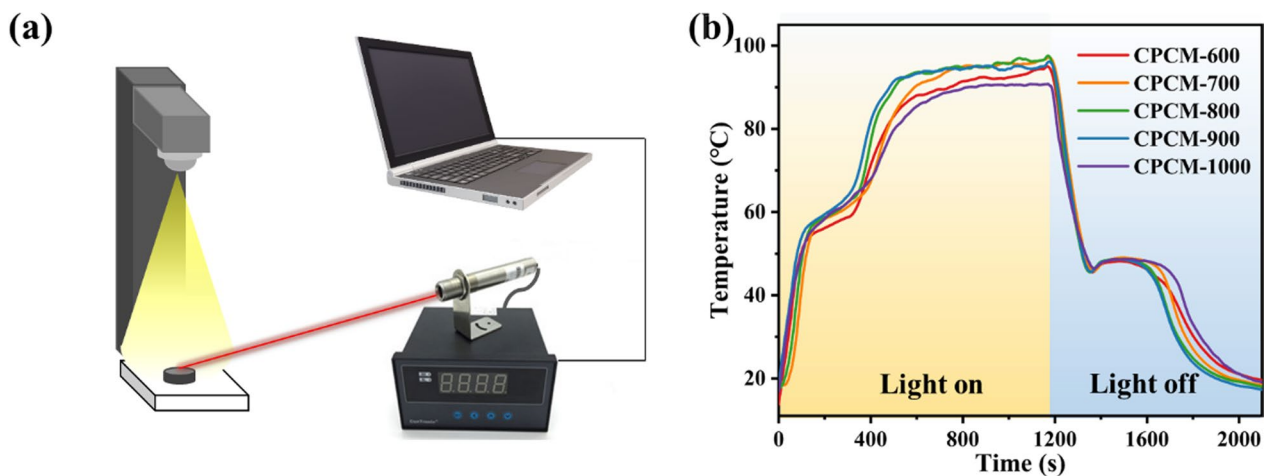
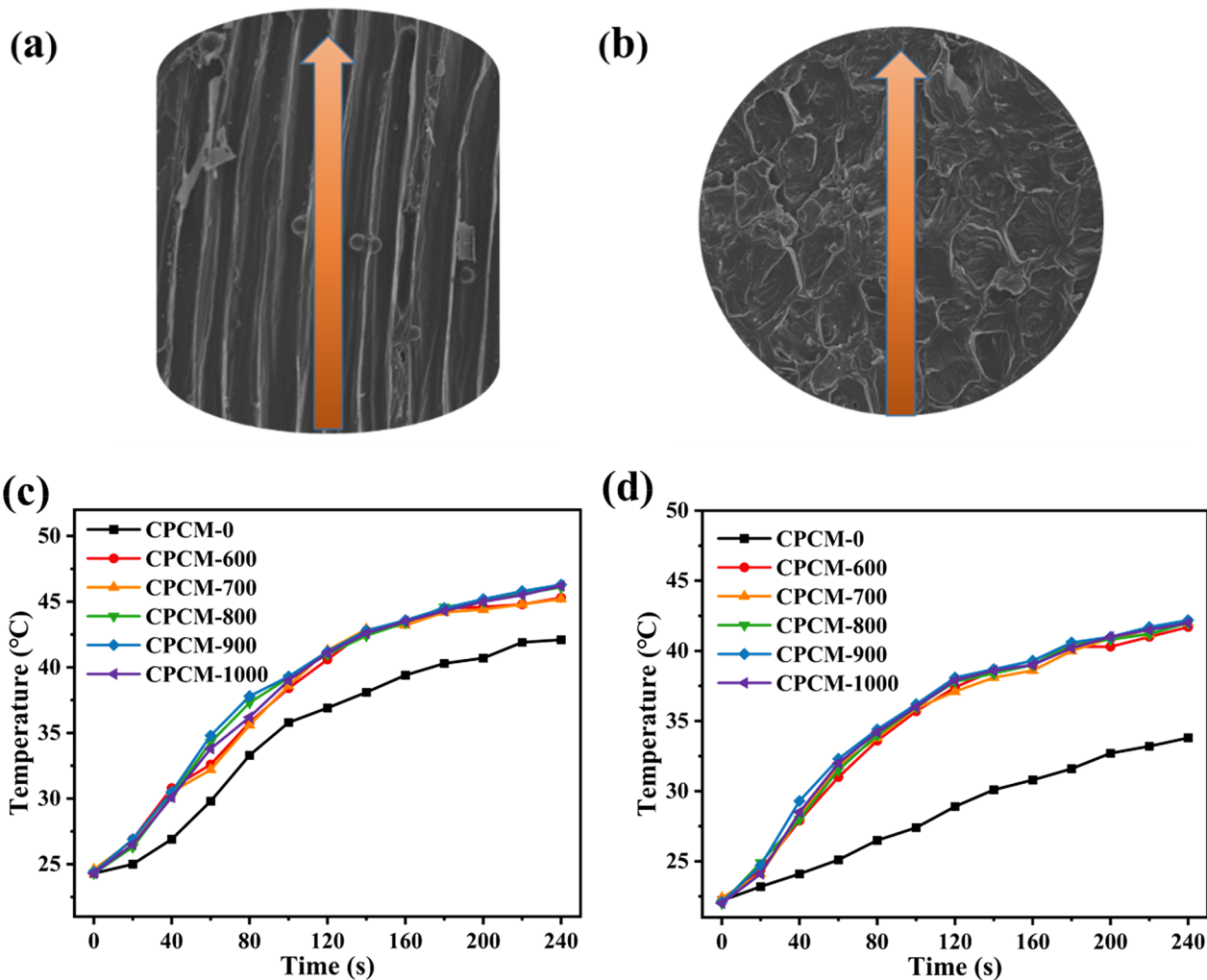


Fig. 10 The solar-to-thermal energy conversion and storage: a The schematic of the measuring system, b Solar-to-thermal conversion curves of CPCM

Table 3 Comparison of the thermal properties of the prepared ss-CPCMs and the biomass-based CPCMs previously reported in the literatures

CPCMs	Max. ratio (wt%)	H_M (J g ⁻¹)	Specific surface area (m ² g ⁻¹)	References
PEG/wood flour	75	108.6	–	Liang et al. (2019)
PFG/towel gourd porous carbon	94.5	164.3	465.9	Song et al. (2020)
PEG/carbonized potato	50	91.8	42.6	Tan et al. (2016)
PEG/pomelo peel foam	96.2	157.9	15.02	Sheng et al. (2020)
PEG/balsa wood	83.5	134	24.7	Meng et al. (2020)
PEG/carbonized diatom	72.7	128.9	155.9	Wu et al. (2021)
PEG/eggplants-derived porous carbon	90.1	149	–	Li et al. (2020a, b, c)
CPCM-900	88.62	170.44	542.25	This work

**Fig. 11** **a** Radial and **b** lateral thermal transfer schematic diagrams of CPCMs, **c** radial and **d** lateral thermal transfer T–t curves per unit length CPCMs

T_f correspond to the time of the start and end of the phase transition. The calculated η for CPCM-600, CPCM-700, CPCM-800, CPCM-900 and CPCM-1000 was 95.93%, 96.68%, 97.33%, 97.70% and 93.47%, respectively. Of these,

CPCM-900 had the highest solar-thermal conversion efficiency. Therefore, biochar-based CPCMs with fast photo-response capability can reduce the limiting effects of climate and environment (Kung and Mu 2019; Tang et al. 2021). In

summary, the biochar-based CPCMs have excellent solar-thermal conversion and storage capacity, with great potential for improving solar energy utilization and in regulating the ambient temperature.

To further investigate the anisotropic structure of CH, the radial and lateral heat transport abilities of CPCMs were tested. The samples with both radial and lateral lengths of 1 cm (Fig. 11a and b) were placed on a heating plate and the ability of CPCMs to conduct heat along the longitudinal and transverse directions was probed by recording the temperature at the top (Li et al. 2021a, b). Figure 11c and d record the temperature changes of CPCMs in the radial and lateral directions during the heating process, respectively. It can be found that the heating rate along the longitudinal direction (parallel to the orifice) was greater than that along the transverse direction (perpendicular to the orifice). The maximum temperature of the radial heat transfer is up to 46 °C, while the maximum temperature of the lateral heat transfer is only 42 °C. Furthermore, the heat transfer capability of CPCMs with biochar as the carrier was much higher than that of CPCM with uncarbonized hemp stem. In general, the hemp stem-derived biochar has good heat transfer capability and its anisotropic structure is also beneficial to broaden the application scope of CPCMs.

4 Conclusions

The ss-CPCMs were prepared by vacuum impregnation using hemp stem-derived biochars as the scaffold and PEG6000 as the PCM. The biochar features a unique anisotropic, graded porous structure with a maximum PEG loading of 88.62wt%. The biochar provides an excellent support material for the preparation of CPCMs and offers a new idea for the efficient utilization of biological waste. Through a series of analyses of thermal stability, thermal material properties, thermal conductivity and light absorption performance it was confirmed that the prepared CPCMs have good thermal reliability, high thermal storage capacity, improved thermal conductivity and excellent solar-thermal conversion capacity. Arrestingly, the CPCMs have a unique anisotropic thermal conductivity, and have promising applications in thermal energy management.

Acknowledgements This work is financially supported by the National Natural Science Foundation of China (51890893), Fundamental Research Funds for the Central Universities (FRF-TP-20-005A3).

Author contributions Methodology, formal analysis and investigation, writing—original draft preparation: RY; resources, methodology, formal analysis and investigation: XG, HW, WK, KS, YL; conceptualization, writing—review and editing, funding acquisition, supervision:

XH; writing—review and editing: GW. All authors read and approved the final manuscript.

Funding This study was supported by the National Natural Science Foundation of China (51890893) and Fundamental Research Funds for the Central Universities (FRF-TP-20-005A3).

Availability of data and materials The datasets analysed during the current study are available from the corresponding author on reasonable request.

Code availability Not applicable.

Declarations

Conflict of interest The authors declared that the research was conducted in the absence of any commercial or financial relationships that could be construed as a potential competing interests.

Consent for publication Not applicable.

Ethical approval and consent to participate Not applicable.

Open Access This article is licensed under a Creative Commons Attribution 4.0 International License, which permits use, sharing, adaptation, distribution and reproduction in any medium or format, as long as you give appropriate credit to the original author(s) and the source, provide a link to the Creative Commons licence, and indicate if changes were made. The images or other third party material in this article are included in the article's Creative Commons licence, unless indicated otherwise in a credit line to the material. If material is not included in the article's Creative Commons licence and your intended use is not permitted by statutory regulation or exceeds the permitted use, you will need to obtain permission directly from the copyright holder. To view a copy of this licence, visit <http://creativecommons.org/licenses/by/4.0/>.


References

- Aftab W, Usman A, Shi J, Yuan K, Qin M, Zou R (2021) Phase change material-integrated latent heat storage systems for sustainable energy solutions. *Energy Environ Sci* 14(8):4268–4291
- Alva G, Liu L, Huang X, Fang G (2017) Thermal energy storage materials and systems for solar energy applications. *Renew Sustain Energy Rev* 68:693–706
- Atinafu DG, Yeol Yun B, Uk Kim Y, Wi S, Kim S (2021) Introduction of eicosane into biochar derived from softwood and wheat straw: influence of porous structure and surface chemistry. *Chem Eng J* 415:128887
- Cao Y, Meng Y, Jiang Y, Qian S, Fan D, Zhou X, Qian Y, Lin S, Qian T, Pan Q (2022) Healable supramolecular phase change polymers for thermal energy harvesting and storage. *Chem Eng J* 433:134549
- Chen C, Ling H, Zhai Z, Li Y, Yang F, Han F, Wei S (2018) Thermal performance of an active-passive ventilation wall with phase change material in solar greenhouses. *Appl Energy* 216:602–612
- Chen X, Cheng P, Tang Z, Xu X, Gao H, Wang G (2021) Carbon-based composite phase change materials for thermal energy storage, transfer, and conversion. *Adv Sci* 8(9):2001274

- Gabhi R, Basile L, Kirk DW, Giorcelli M, Tagliaferro A, Jia CQ (2020) Electrical conductivity of wood biochar monoliths and its dependence on pyrolysis temperature. *Biochar* 2(3):369–378
- Guo N, Li M, Wang Y, Sun X, Wang F, Yang R (2016) N-Doped hierarchical porous carbon prepared by simultaneous-activation of KOH and NH₃ for high performance supercapacitors. *RSC Adv* 6(103):101372–101379
- Huang Q, Song S, Chen Z, Hu B, Chen J, Wang X (2019a) Biochar-based materials and their applications in removal of organic contaminants from wastewater: state-of-the-art review. *Biochar* 1(1):45–73
- Huang XB, Chen X, Li A, Atinafu D, Gao HY, Dong WJ, Wang G (2019b) Shape-stabilized phase change materials based on porous supports for thermal energy storage applications. *Chem Eng J* 356:641–661
- Kim M, Fernando JFS, Li Z, Alowasheer A, Ashok A, Xin R, Martin D, Kumar Nanjundan A, Golberg DV, Yamauchi Y, Amiralian N, Li J (2022) Ultra-stable sodium ion storage of biomass porous carbon derived from sugarcane. *Chem Eng J* 445:136344
- Kung C-C, Mu JE (2019) Prospect of China's renewable energy development from pyrolysis and biochar applications under climate change. *Renew Sustain Energy Rev* 114:109343
- Kung C-C, McCarl BA, Chen C-C, Cao X (2014a) Environmental impact and energy production: evaluation of biochar application on Taiwanese set-aside land. *Energy Environ* 25(1):13–39
- Kung C-C, Xie H, Wu T, Chen S-C (2014b) Biofuel for energy security: an examination on pyrolysis systems with emissions from fertilizer and land-use change. *Sustainability* 6(2):571–588
- Kung C-C, Kong F, Choi Y (2015) Pyrolysis and biochar potential using crop residues and agricultural wastes in China. *Ecol Indic* 51:139–145
- Li J, Jiang Q, Wei L, Zhong L, Wang X (2020a) Simple and scalable synthesis of hierarchical porous carbon derived from cornstalk without pith for high capacitance and energy density. *J Mater Chem A* 8(3):1469–1479
- Li YQ, Huang XB, Li Y, Xi ZS, Hai GT, Tao Z, Wang G (2020b) Shape-stabilized phase-change materials supported by eggplant-derived porous carbon for efficient solar-to-thermal energy conversion and storage. *Sustain Energy Fuels* 4(4):1764–1772
- Li Y, Li YQ, Huang XB, Zheng HY, Lu GL, Xi ZS, Wang G (2020c) Graphene-CoO/PEG composite phase change materials with enhanced solar-to-thermal energy conversion and storage capacity. *Compos Sci Technol* 195:108197
- Li J, Hu X, Zhang C, Luo W, Jiang X (2021a) Enhanced thermal performance of phase-change materials supported by mesoporous silica modified with polydopamine/nano-metal particles for thermal energy storage. *Renew Energy* 178:118–127
- Li YQ, Chen YM, Huang XB, Jiang SH, Wang G (2021b) Anisotropy-functionalized cellulose-based phase change materials with reinforced solar-thermal energy conversion and storage capacity. *Chem Eng J* 415:129086
- Li YQ, Huang XB, Hai GT, Lv JJ, Tao Z, Wang G (2022a) Crystallization of C18 in mesoporous silica: effect of surface functionalization and nanoconfinement. *Chem Eng J* 428:131075
- Li YQ, Huang XB, Lv JJ, Wang F, Jiang SH, Wang G (2022b) Enzymolysis-treated wood-derived hierarchical porous carbon for fluorescence-functionalized phase change materials. *Compos Part B* 234:109735
- Liang B, Lu X, Li R, Tu W, Yang Z, Yuan T (2019) Solvent-free preparation of bio-based polyethylene glycol/wood flour composites as novel shape-stabilized phase change materials for solar thermal energy storage. *Sol Energy Mater Sol Cells* 200:110037
- Meng Y, Majoinen J, Zhao B, Rojas OJ (2020) Form-stable phase change materials from mesoporous balsa after selective removal of lignin. *Compos Part B* 199:108296
- Oginni O, Singh K (2020) Influence of high carbonization temperatures on microstructural and physicochemical characteristics of herbaceous biomass derived biochars. *J Environ Chem Eng* 8(5):104169
- Pan X, Zhang N, Yuan Y, Shao X, Zhong W, Yang L (2021) Balsa-based porous carbon composite phase change material with photo-thermal conversion performance for thermal energy storage. *Sol Energy* 230:269–277
- Peng B, Xu Y, Liu K, Wang X, Mulder FM (2017) High-performance and low-cost sodium-ion anode based on a facile black phosphorus-carbon nanocomposite. *ChemElectroChem* 4(9):2140–2144
- Qiu D, Kang C, Gao A, Xie Z, Li Y, Li M, Wang F, Yang R (2019) Sustainable low-temperature activation to customize pore structure and heteroatoms of biomass-derived carbon enabling unprecedented durable supercapacitors. *ACS Sustain Chem Eng* 7(17):14629–14638
- Rathore PKS, Sk S (2021) Improvement in thermal properties of PCM/Expanded vermiculite/expanded graphite shape stabilized composite PCM for building energy applications. *Renew Energy* 176:295–304
- Sari A, Hekimoğlu G, Tyagi VV (2020) Low cost and eco-friendly wood fiber-based composite phase change material: development, characterization and lab-scale thermoregulation performance for thermal energy storage. *Energy* 195:116983
- Sheng X, Dong D, Lu X, Zhang L, Chen Y (2020) MXene-wrapped bio-based pomelo peel foam/polyethylene glycol composite phase change material with enhanced light-to-thermal conversion efficiency, thermal energy storage capability and thermal conductivity. *Compos A* 138:106067
- Shi Y, Gerkman MA, Qiu Q, Zhang S, Han GGD (2021) Sunlight-activated phase change materials for controlled heat storage and triggered release. *J Mater Chem A* 9(15):9798–9808
- Song J, Cai Y, Du M, Hou X, Huang F, Wei Q (2020) 3D lamellar structure of biomass-based porous carbon derived from towel gourd toward phase change composites with thermal management and protection. *ACS Appl Bio Mater* 3(12):8923–8932
- Tan B, Huang Z, Yin Z, Min X, Liu YG, Wu X, Fang M (2016) Preparation and thermal properties of shape-stabilized composite phase change materials based on polyethylene glycol and porous carbon prepared from potato. *RSC Adv* 6(19):15821–15830
- Tang Z, Gao H, Chen X, Zhang Y, Li A, Wang G (2021) Advanced multifunctional composite phase change materials based on photo-responsive materials. *Nano Energy* 80:105454
- Tomizawa Y, Sasaki K, Kuroda A, Takeda R, Kaito Y (2016) Experimental and numerical study on phase change material (PCM) for thermal management of mobile devices. *Appl Therm Eng* 98:320–329
- Tong X, Li N, Zeng M, Wang Q (2019) Organic phase change materials confined in carbon-based materials for thermal properties enhancement: Recent advancement and challenges. *Renew Sustain Energy Rev* 108:398–422
- Umair MM, Zhang Y, Iqbal K, Zhang S, Tang B (2019) Novel strategies and supporting materials applied to shape-stabilize organic phase change materials for thermal energy storage—a review. *Appl Energy* 235:846–873
- Umair MM, Zhang Y, Tehrim A, Zhang S, Tang B (2020) Form-stable phase-change composites supported by a biomass-derived carbon scaffold with multiple energy conversion abilities. *Ind Eng Chem Res* 59(4):1393–1401
- Wang JJ, Huang XB, Gao HY, Li A, Wang C (2018) Construction of CNT@Cr-MIL-101-NH₂ hybrid composite for shape-stabilized

- phase change materials with enhanced thermal conductivity. *Chem Eng J* 350:164–172
- Wang W, Umair MM, Qiu J, Fan X, Cui Z, Yao Y, Tang B (2019) Electromagnetic and solar energy conversion and storage based on Fe₃O₄-functionalised graphene/phase change material nanocomposites. *Energy Convers Manage* 196:1299–1305
- Wu B, Lyu S, Han H, Li T, Sun H, Wang J-K, Li D, Lei F, Huang J, Sun D (2021) Biomass-based shape-stabilized phase change materials from artificially cultured ship-shaped diatom frustules with high enthalpy for thermal energy storage. *Compos Part B* 205:108500
- Yang J, Tang LS, Bao RY, Bai L, Liu ZY, Xie BH, Yang MB, Yang W (2018) Hybrid network structure of boron nitride and graphene oxide in shape-stabilized composite phase change materials with enhanced thermal conductivity and light-to-electric energy conversion capability. *Sol Energy Mater Sol Cells* 174:56–64
- Yang J, Tang LS, Bai L, Bao RY, Liu ZY, Xie BH, Yang MB, Yang W (2019) High-performance composite phase change materials for energy conversion based on macroscopically three-dimensional structural materials. *Mater Horiz* 6(2):250–273
- Yuan M, Xu C, Wang T, Zhang T, Pan X, Ye F (2021) Supercooling suppression and crystallization behaviour of erythritol/expanded graphite as form-stable phase change material. *Chem Eng J* 413:127394
- Zhang X, Huang Z, Yin Z, Zhang W, Huang Y, Liu Y, Fang M, Wu X, Min X (2017) Form stable composite phase change materials from palmitic-lauric acid eutectic mixture and carbonized abandoned rice: preparation, characterization, and thermal conductivity enhancement. *Energy Build* 154:46–54
- Zhang W, Zhang X, Zhang X, Yin Z, Liu Y, Fang M, Wu X, Min X, Huang Z (2019) Lauric-stearic acid eutectic mixture/carbonized biomass waste corn cob composite phase change materials: preparation and thermal characterization. *Thermochim Acta* 674:21–27
- Zhang C, Hu X, Xiao S, Luo W, Wang H, Jiang X (2021a) Enhanced thermal performance of phase-change material supported by nano-Ag coated eggplant-based biological porous carbon. *J Energy Storage* 43:103174
- Zhang H, Wang L, Xi S, Xie H, Yu W (2021b) 3D porous copper foam-based shape-stabilized composite phase change materials for high photothermal conversion, thermal conductivity and storage. *Renew Energy* 175:307–317
- Zhao Y, Min X, Huang Z, Liu YG, Wu X, Fang M (2018) Honeycomb-like structured biological porous carbon encapsulating PEG: a shape-stable phase change material with enhanced thermal conductivity for thermal energy storage. *Energy Build* 158:1049–1062
- Zhou M, Wang J, Zhao Y, Wang G, Gu W, Ji G (2021) Hierarchically porous wood-derived carbon scaffold embedded phase change materials for integrated thermal energy management, electromagnetic interference shielding and multifunctional application. *Carbon* 183:515–524

Authors and Affiliations

Ruiying Yang¹ · Xiran Guo¹ · Haotian Wu¹ · Weizhi Kang¹ · Kun Song¹ · Yaqiong Li¹ · Xiubing Huang¹  · Ge Wang¹

✉ Xiubing Huang
xiubinghuang@ustb.edu.cn

✉ Ge Wang
gewang@ustb.edu.cn

¹ Beijing Key Laboratory of Function Materials for Molecule and Structure Construction, School of Materials Science and Engineering, University of Science and Technology Beijing, Beijing 10083, People's Republic of China